Gold Nanoparticle Flow Sensors Designed for Dynamic X-ray Imaging in Biofluids

Sungsook Ahn, Sung Yong Jung, Jin Pyung Lee, Hae Koo Kim, and Sang Joon Lee*

Center for Biofluid and Biomimic Research, Department of Mechanical Engineering, Pohang University of Science and Technology (POSTECH), San 31, Hyoja Dong, Namgu, Pohang 790-784, Korea

ARTICLE

ABSTRACT X-ray-based imaging is one of the most powerful and convenient methods in terms of versatility in applicable energy and high performance in use. Different from conventional nuclear medicine imaging, contrast agents are required in X-ray imaging especially for effectively targeted and molecularly specific functions. Here, in contrast to much reported static accumulation of the contrast agents in targeted organs, dynamic visualization in a living organism is successfully accomplished by the particle-traced X-ray imaging for the first time. Flow phenomena across perforated end walls of xylem vessels in rice are monitored by a gold nanoparticle (AuNP) (~20 nm in diameter) as a flow tracing sensor working in nontransparent biofluids. AuNPs are surface-modified to control the hydrodynamic properties such as hydrodynamic size (D_H), ζ-potential, and surface plasmonic properties in aqueous conditions. Transmission electron microscopy (TEM), scanning electron microscopy (SEM), X-ray nanoscopy (XN), and X-ray microscopy (XM) are used to correlate the interparticle interactions with X-ray absorption ability. Cluster formation and X-ray contrast ability of the AuNPs are successfully modulated by controlling the interparticle interactions evaluated as flow-tracing sensors.

KEYWORDS: dynamic X-ray imaging · gold nanoparticle (AuNP) · contrast agents · smart materials · self-assembly · xylem vessel · sap flow

Monitoring an *in situ* fluid flow in a living organism is an essential technology to understand the dynamic processes controlling life phenomenon. In this point of view, velocity measurement in biological fluids is one of the key technologies in detecting and treating circulatory diseases related with abnormal flows.[1,2] Particle image velocimetry (PIV) or particle tracking velocimetry (PTV) technique has been established as a reliable velocity field measurement where detectable flow tracers represent the stream motions as a function of time. However, biological organisms are usually opaque, thus the measurement of the dynamic flows in biofluids encounters serious obstacles. To see through the internal structures of those opaque samples, X-ray imaging technologies have been utilized over the last decades.[3,4] In the combined X-ray PIV (or X-ray PTV) technique, quantitative information on opaque biofluids can be obtained,[5,6] where the tracer particles need to have effective contrast against the surrounding medium.

The X-ray absorption efficiency of gold (Au) is about 2.7 times higher (5.16 cm^2/g at 100 KeV) than that of commonly used X-ray contrast agent, iodine (1.94 cm^2/g at 100 KeV).[7] The X-ray attenuation coefficient of Au is even 150-fold higher than that of bone (0.186 cm^2/g at 100 KeV) and soft tissue (0.169 cm^2/g at 100 KeV). The gold nanoparticles (AuNPs) injected intravenously were reported to accumulate in organs such as the liver.[8] In addition, AuNPs are typically regarded as a biocompatible material.[9] With unique surface plasmon oscillations,[10] AuNPs have been employed extensively for biosensing[11] and cancer imaging[12] in biological and medical applications. Especially in particle-traced imaging technology, gold can be shaped into particles with versatile sizes and shapes. This is one of the great advantages of gold as a tracing sensor since the typical liquid form of X-ray contrast agent (such as iodine) cannot generate discrete positional information on the image.[13] Considering increased endocytosis, proper biodistribution, and potential clearance from living organisms, the optimal hydrodynamic sizes (D_H) of the AuNPs were reported to be in the range of 20−50 nm.[8] Recent developments in nano- and biotechnology require more integrated understanding over the biological interactions in conjunction with the applied engineered materials.[14] Studying the interplay of fine tracer particles with the surrounding medium is a prerequisite for analyzing their dynamic behaviors. In this point of view, the physical properties of the particles, such as size, shape, surface functionality, surface charge, and solvophilicity, are the important factors under a given medium condition.[15,16]

*Address correspondence to sjlee@postech.ac.kr.

Received for review January 24, 2010 and accepted June 24, 2010.

Published online July 1, 2010.
10.1021/nn1003293

The cohesion-tension theory[17,18] is one of the most widely accepted viewpoints to explain the ascent of sap in vascular plants. The driving force of the ascent of sap flow was reported to be generated by the surface tension on the leaf where water evaporates and the formation of a hydrostatic pressure gradient over a continuous water column within the rigid xylem vessels of a plant. Many controversies still remain over the opposed theoretical viewpoints because direct measurements of the sap flow within the xylem vessels are still limited. The direct visualization of the ascent of sap in vascular plants has a number of problems due to the presence of thick and porous cell walls and the complicated structure of the xylem vessels. Lee *et al.*[19] recently studied the refilling process of the sap in xylem vessels using an X-ray microimaging technique by tracing the menisci between air and sap liquids. However, this experimental technique requires cutting off plant sections and generating air/water interface artificially. Among the anatomical features of xylem vessels, perforation plates at end walls of vessels and bordered pit membranes represent physical barriers to sap flow. They are constituted by hydrolyzed cell walls composed of a cellulose microfibril network noncovalently bound to a cell wall matrix. The variations in the physicochemical conditions of the perforation plates and pit membranes, including porosity and pore size (from a few nanometers to tens of micrometers), mediated by ionic compositions of the xylem sap are one of the essential clues to understand the whole metabolism of plants.[20,21]

The interactions between nanoparticles and plants are not fully understood yet. In particular, the uptake and accumulation process of nanoparticles and their biological impact on the plant structure and biochemical processes also remain an open questions. Corredor *et al.*[22] have analyzed the penetration and movement of iron−carbon nanoparticles in *Cucurbita pepo* cells, by which magnetic nanoparticles penetrate into a plant and travel through the whole vascular system. Nanoparticles with a diameter larger than 50 nm have not been detected inside a plant tissue. This indicates that a size-based filtering mechanism seems to work. The use of nanoparticles for targeted delivery of substances has received special attention especially related to disease treatment. To the best of our knowledge, there is little *in vivo* experiments that visualize the penetration and transport of AuNPs inside the xylem vessels. The AuNPs developed in this study are around 20 nm in diameter, and the high X-ray absorption of gold generates effective contrast suitable for the *in vivo* exploration of xylem sap flow by the penetrable X-ray imaging technique.

Nanoparticles are supposed to penetrate into biological systems typically across the membranes of unique size and structure in nanometer scale. Until now, even with the most updated X-ray PIV technique, nanoparticles of 20 nm in diameter could not be detected as a single point.[6] Therefore, contrast agents need to be large enough to obtain proper intensity contrasted from the transmitted X-ray, and simultaneously, their sizes have to be small enough to pass through the unique structure of a membrane. In this study, a suitable aggregation of ~20 nm AuNPs is suggested where the interactive behaviors of AuNPs coated with diversified shells are compared. To produce high enough absorption in the X-ray images, aggregation of the particle is effectively induced by controlling the particle-to-particle interaction. Therefore, the X-ray absorption rate is noticeably optimized by the AuNP clusters to make the time-dependent flow measurement possible.

RESULTS AND DISCUSSION

Surface-Modified AuNPs. In this study, ligands of low molecular weight are covered on the surface of AuNPs. This methodology has two advantages over the polymeric surface protectors. First, by reducing the shell thickness (*i.e.*, the core-to-core distance among the particles), the Au density could increase, thus the unnecessary components for the X-ray absorption are minimized. Second, by shortening the length from the Au surface to the functional end group of the ligand, the spacer-dominating packing effect could be diminished.[23] As a ligand attached on the Au surface, thionic compounds are known to bind to Au strongly because of the soft character of both Au and S.[24] In this study, a two-step synthesis method is employed to keep the physical size of the Au core similar in all the AuNPs by controlling the particle size with the S to Au ratio and only to modify the surface characteristics. Therefore, the nonuniformity in size is also reduced by the two-step synthesis procedure. The Au crystal is nucleated in a coordinating solvent growing into a nanoparticle to a final size with the help of a reducing agent. Then, the ligands are attached onto the surface of the AuNPs subsequently. In preparing the Au core, gold chloride (III) trihydrate ($HAuCl_4 \cdot 3H_2O$) is dissolved in deionized (DI) Milli-Q water (1.0×10^{-3} mol/L) under refluxing. Sodium citrate tribasic dihydrate solution in DI water (4×10^{-2} mol/L) is added to the above solution according to the conventional Turkevich method.[25] The concentration of Au^{3+} itself and the ratio of Au^{3+} to the reducing agent are the important factors in controlling the final size of the AuNPs.[26] The reaction completion can be detected by the changes in color from pale yellow to wine red. Boiling condition was further maintained for 15 min after the color change is completed followed by cooling to room temperature. The final AuNP solution is dialyzed overnight using Spectra/Por7 membrane (1000 Da cut) against Milli-Q DI water to remove excess sodium citrate tribasic dihydrate. Contrary to the one-step synthesis,[20] thiol ligand is added at the second step. After the size of the AuNP is determined, to modify the surface properties of the citrate-covered

AuNP (AuNP **1**), 40 μL of 0.1 M ligand aqueous solutions is added to the above aqueous solution: thioglycolic acid (SH−CH_2COOH) (AuNP **2**), 4-mercaptobenzoic acid (SH−Ph−COOH) (AuNP **3**), 6-thioguanine (SH−$C_5H_4N_5$) (AuNP **4**), 2-mercaptoethanol (SH−CH_2CH_2OH) (AuNP **5**), and 1-propanthiol (SH−$CH_2CH_2CH_3$) (AuNP **6**) are added and stirred at room temperature or between 50 and 60 °C for 6−12 h until there is no more change in color. Obtained AuNP solutions are dialyzed overnight by Spectra/Por7 membrane (1000 Da cut) against Milli-Q water for purification. In Figure 1a, each AuNP image is captured using transmission electron microscopy (TEM) (JEOL Cs-corrected HR-TEM (JEM-2200FS) for AuNPs **1**−**6**. AuNP solutions are placed on a typical copper grid and then dried under air at room temperature. Since the organic layers of the AuNPs are not clearly detected by the electron beam in TEM, gold cores with high electron density in each AuNP are captured obviously. From this image, the average diameter of the fabricated AuNPs is confirmed at around 20 nm regardless of the type of the ligands.

Solution Properties of AuNPs. Considering the volume of a Au atom (about 17 Å^3), the number of Au atoms in a spherical particle with 10 nm radius (r) is approximately a quarter of a million by the relation $N_{Au} = 4\pi(r)^3/3v_{Au}$ (v_{Au} is the volume of a Au atom = 17 Å^3). On the basis of the Au concentration ($HAuCl_4$, 1.0×10^{-3} mol/L), the average number density of AuNPs in a solution is around 2.4×10^{18} AuNPs/m^3. This implies that approximately 10^{22} nm^3 ($V_{particle}$) is occupied by the AuNPs per cubic meter ($V_{total} = 10^{27}$ nm^3) producing 10^{-5} volume fraction ($\Phi_{particle} = V_{particle}/V_{total}$). If AuNPs are homogeneously dispersed in a medium by the maximum dispersion energy and the thickness of the surface ligand is negligible, the surface-to-surface distance of the AuNP is almost infinite compared with the particle size. Under these conditions, van der Waals force (F_{van}) is expected to become dominant by the relation $F_{van} \sim D^{-6}$, where D is the particle diameter.[27] The unique colors of the AuNP solutions are attributed to the broad absorption band in the visible wavelength region, resulting from the collective oscillations of the electron clouds on the AuNP surface. These unique surface plasmonic resonances in AuNPs are influenced by the size, shape, surface charge, and refractive index of the AuNPs as well as the temperature and the dielectric constant of the medium, *etc.*[28−30] The refractive index of the solvent shifts the surface plasmonic resonances according to the Mie theory;[31] in addition, the change in the refractive index of the AuNP by the ligand shell also affects the energy bands. The strong ligand interaction with the surface electron cloud is expected to modulate the energy band of the surface plasmon significantly.[32]

Figure 1b shows the absorption spectra of the designed AuNPs from **1** to **6** dispersed in DI water, together with the picture images of the solutions. AuNPs **1** and **2** exhibit deep red color, while AuNPs **3** and **5** express bluish red color. AuNPs **4** and **6**, on the other hand, have an apparently bluish color. The absorption is measured by a UV−vis spectrometer (HP, HP8453). AuNPs **1** and **2** have a clear dominant peak at about 524 nm, but the intensity of the peak is lower in AuNP **2**. That main peak is slightly red-shifted to 527 nm in AuNP **3**. Hydrophilic alcohol-functionalized AuNP **5** shows the main absorption peak approximately at 529 nm with lower intensity. Meanwhile, the main peaks of 6-thioguanine- (AuNP **4**) and methyl-covered (AuNP **6**) AuNPs are positioned at around 537 nm with far lower intensity. The absorbance of AuNPs **5** and **6** gradually increases with the increase in the wavelength. AuNP **5** exhibits a prominent peak at around 770 nm. Overall, the absorbance intensity of the main peaks (~520 nm) is decreased with a peak broadening and red-shifted as the surface ligand becomes neutral and/or hydrophobic.

The effective charge formed on the particle surface causes repulsive interactions among the particles. Citrate-covered AuNP **1** is apparently ionized with a negative charge, and glycolic-acid-covered AuNP **2** also can be ionized in DI water because of the relatively low pK_a of glycolic acid (3.86).[33] Meanwhile, due to the pK_a of benzoic acid (4.2) and 6-thioguanine (8.26),[34] AuNPs **3** and **4** are supposed to be less effectively ionized compared with AuNPs **1** and **2**. AuNPs **1** and **2** do not exhibit any noticeable peak at higher wavelengths beyond the clear main peak at 524 nm. However, AuNPs **4** and **6** show broad second peaks at higher wavelength, which indicates effective aggregation of AuNPs. AuNPs **1** and **2** show an almost similar pattern in absorbance. However, the intensity of AuNP **2** is smaller than that of AuNP **1**, attributed to relatively more effective ionization of citrate than glycolic acid, where the negative charge of COO^- is replaced by neutral COOH. The hydrophobic association of the phenyl group in AuNP **3** contributes to the slight red shift and peak broadening. The internal hydrogen bonding of the amine group in AuNP **4** and the hydrophobic surface in AuNP **6** are supposed to promote prominent particle aggregation, leading to a rather moderate absorption at higher wavelengths in a broad range. However, the hydrophilic AuNP **5** exhibits sharp absorption at the second peak, which reflects the regularly structured aggregates stably dispersed in DI water.

The hydrodynamic sizes (D_H) of fabricated AuNPs dispersed in various solvents are measured using photon correlation spectroscopy (PCS) (Zetasizer Nano S, Malvern Instruments, Worcestershire, U.K.). The surface charge is determined by ζ-potential measured by a laser Doppler electrophoresis (LDE) (Zetasizer Nano Z, Malvern Instruments, Worcestershire, U.K.). Each measurement is carried out at 25 °C, and data sets of 40 runs are averaged to obtain the mean value. The D_H of the

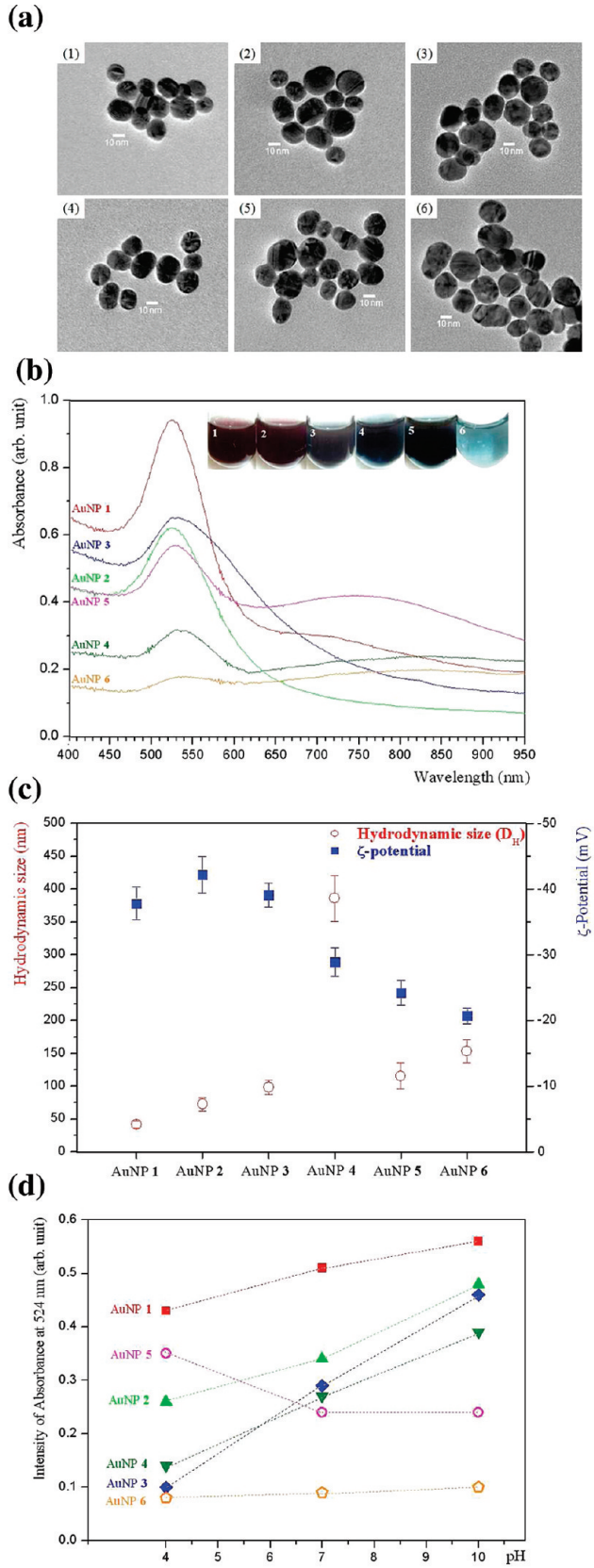

Figure 1. Characteristics of six AuNPs in this study. (a) Transmission electron microscopy (TEM) images of AuNPs. Each AuNP is covered with (1) citrate (AuNP 1), (2) thioglycolic acid (SH−CH_2COOH) (AuNP 2), (3) 4-mercaptobenzoic acid (SH−Ph−COOH) (AuNP 3), (4) 6-thioguanine (SH−$C_5H_4N_5$) (AuNP 4), (5) 2-mercaptoethanol (SH−CH_2CH_2OH) (AuNP 5), and (6) 1-propanthiol (SH−$CH_2CH_2CH_3$) (AuNP 6). Scale bar is 10 nm. (b) UV−vis absorption spectra and picture of the six AuNP solutions in DI water. (c) Hydrodynamic size (D_H) and ζ-potential of the AuNP solutions in DI water. (d) Absorption intensity of the main peak (around 520 nm shown in panel b) at different pH conditions.

particle is related to the movement of the particles in a specific medium expressed by the Stokes−Einstein equation,[35] where the charge layer and surface coatings of the particles need to be considered. Outside the strong electrical layer composed of the opposite charge of the particle body (Stern layer), a diffuse layer is generated by the electrical field ranging from the highly charged particle surface to the almost infinite end of the diffuse layer. The ζ-potential is defined as the electrical potential of the ions which move together with the particle body, thus each particle is individually discernible as a single entity. Therefore, both the D_H and ζ-potential of the particles are strongly influenced by the media condition.[35]

The variations in the D_H and the ζ-potential of the particles are shown in Figure 1c. From AuNPs **1** to **6**, the D_H increases (AuNP **4** is far higher over the other particles), while the ζ-potential decreases overall. This implies that the particle interactions are dominated by the ζ-potential of the particles, where the high surface charge of the particles leads to effective particle separation induced by electrostatic repulsion. The D_H of AuNP **1** is almost twice of the physical size of the AuNP (∼20 nm in diameter) observed in the aforementioned TEM. This implies the dominating pair interaction of citrate-covered AuNPs. Meanwhile, AuNPs **2**, **3**, **5**, and **6** show cluster formation composed of several particles on average. The AuNP **4** exhibits far more effective cluster formation in DI water, possibly due to relatively high molecular weight and effective internal hydrogen bonding of 6-thioguanine. The ζ-potential decreases in AuNPs **3** and **4** and further more in AuNPs **5** and **6**. This indicates the AuNPs **5** and **6** are almost ineffective in charge ($<\pm$30 mV) with neutral ligands.

Figure 1d compares the intensity variations of the main plasmonic peaks (that appear at around 524−529 nm) in each AuNP system at different pH conditions. Affected by the ionic interactions in the pH-controlled buffer solutions, all AuNP systems exhibit prominently decreased intensity compared with those in DI water. This results from the effective aggregation of AuNPs. The intensity of the plasmonic absorbance has smaller values at pH 4 and increases gradually up to pH 10 from AuNP **1** to **4**. AuNP **4** containing amine groups also exhibits increased intensity at pH 10 compared with those at pH 4 and pH 7. When we consider the pK_a of 6-thioguanine (8.26), the negative charge (or neutral) at higher pH would be more beneficial than the positive charge at lower pH (and even in DI water condition) in terms of particle stability. In the meantime, the plasmonic intensity of AuNPs **5** and **6** with neutral ligands does not increase at higher pH conditions. In the case of AuNP **5**, the intensity even decreases at higher pH, due to possible ionization of the hydroxyl groups at lower pH conditions (H_3O^+).

Self-Assembly of AuNPs. In Figure 2, the packing arrangements of single AuNPs are obtained in nano- and microscale using scanning electron microscopy (SEM) (JEOL JSM-7401F SEM at an acceleration voltage of 15 kV) and zone-plate X-ray nanoscopy (XN).[36] AuNP solutions are placed on a silicon nitride membrane for SEM and XN, and the solvent is then evaporated. Regardless of the type of the AuNPs designed in this study, the single particle has an average physical diameter of ∼20 nm. However, in a zoomed-out scale, the arrangements of the AuNPs are characteristically different depending on the ligand type. In a solution state, the particle-to-solvent interaction ($\chi_{p\text{-}s}$) competes with that of the particle-to-particle ($\chi_{p\text{-}p}$), which can be quantified by the Flory−Huggins interaction parameter, χ. During the solvent evaporation procedure, the particles are congested in limited spaces where the particle-to-particle interaction becomes more important. Hamaker[27] expressed the interaction energy (E) between the spheres with a finite volume as a function of separation distance. With D_1 and D_2 being the diameters of particles 1 and 2 and d the surface-to-surface distance between the two particles, the interaction can be expressed as a function of the particle diameter and interparticle distance as follows:

$$E(D) = -A_H/12\{y/(x^2+xy+x) + y/(x^2+xy+x+y) + 2\ln[(x^2+xy+x)/(x^2+xy+x+y)]\} \quad (1)$$

where $x = d/2R_1 = d/D_1$, $y = D_2/D_1 = R_1/R_2$, and A_H is the material-dependent Hamaker constant (1.95 eV for Au−Au attraction).[27] Assuming that the sizes of the two interacting particles are identical ($D_1 = D_2 = D$), y becomes unity. The Hamaker formalism is thus simplified into

$$E(D) = -A_H/12\{1/(x(x+2) + 1/(x+1)^2 + 2\ln[(x(x+2)/(x+1)^2]\} \quad (2)$$

Therefore, the ratio of the particle-to-particle distance (d) to the particle diameter (D) mainly controls the interaction energy. When $x \gg 1$, the above relation becomes

$$E(D) = -A_H/24x = -A_H D/24d \quad (3)$$

As the diameter of the AuNPs fabricated in this study can be suggested to be fixed ($D \cong 20$ nm), the dispersing energy is inversely proportional to the surface-to-surface distance (d) in linear relation. From the SEM images, the average number of particle (N_{av}) is counted at several regions of a 200 × 200 nm^2 area. The average surface-to-surface particle distance (d_{av}) can be obtained from the following relation

$$d_{av} = [1 - \pi(D/2)^2 f_{av}]^{1/2} \quad (4)$$

where f_{av} is the number fraction of the particle.

The cluster formation of the particles in nanoscale is exhibited in the SEM images in Figure 2a. From those images, the average number of particles in the selected

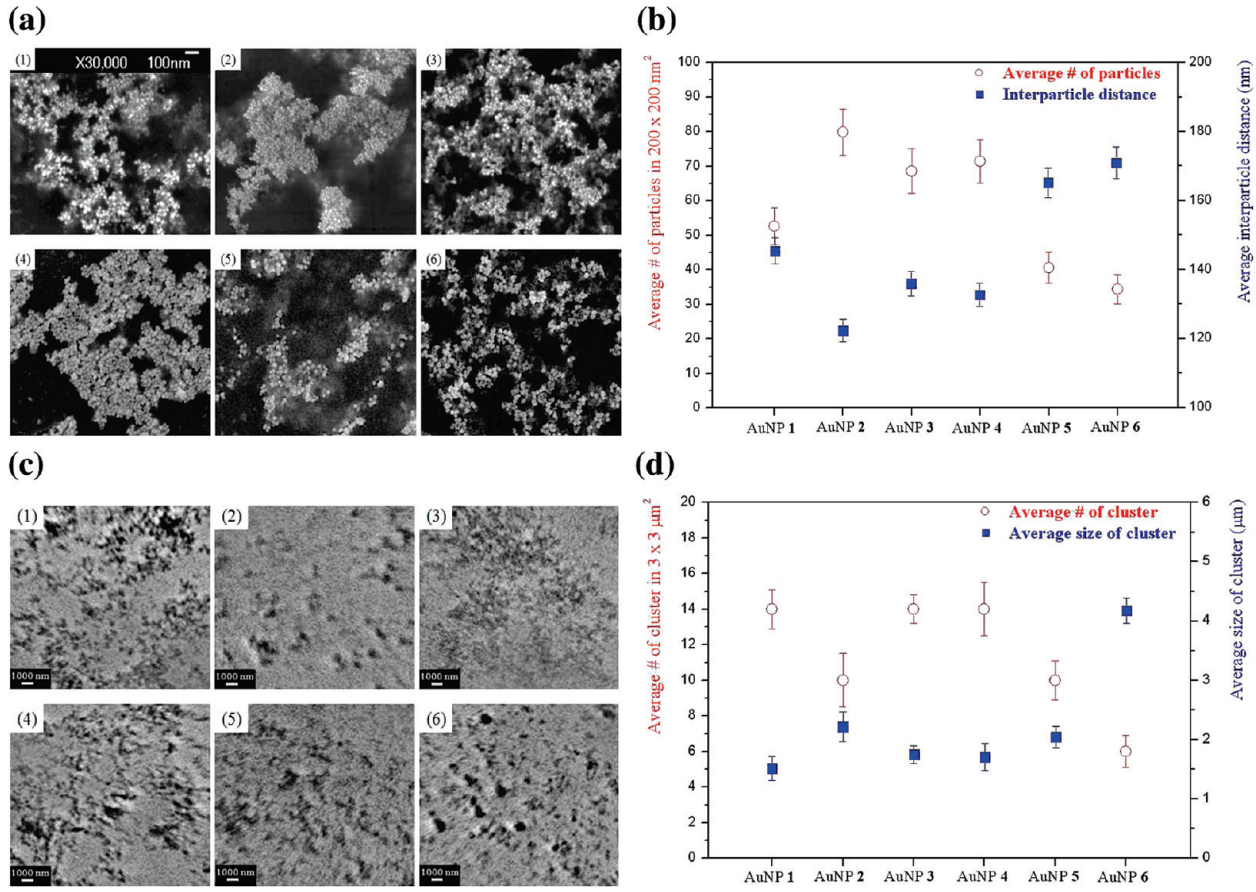

Figure 2. Clusters of the six AuNPs in this study. (a) Scanning electron microscopy (SEM) images. (1) AuNP 1, (2) AuNP 2, (3) AuNP 3, (4) AuNP 4, (5) AuNP 5m and (6) AuNP 6. Scale bar is 100 nm. (b) Average number of AuNPs counted in a 200 × 200 nm² area and their interparticle distances. (c) Zone-plate X-ray nanoscopy (XN) images: (1) AuNP 1, (2) AuNP 2, (3) AuNP 3, (4) AuNP 4, (5) AuNP 5, and (6) AuNP 6. Scale bar is 1000 nm. (d) Average number of AuNP clusters counted in a 3 × 3 μm² area and their average size.

areas and the obtained interparticle distances (d_{av}) are presented in Figure 2b. The two values exhibit symmetric variations. The tendency of d_{av} is opposite to the hydrodynamic size (D_H) previously observed in Figure 1c. Different from the D_H, the d_{av} of AuNP **4** is not exceptionally high. The d_{av} values of AuNPs **2**−**4** are significantly lower than that of AuNP **1**. Therefore, compared with the citrate-covered AuNP **1**, the glycolic-acid-covered AuNP **2** has an effective particle attraction generated by the possible hydrogen bonding between the AuNPs. The benzoic-acid-covered AuNP **3** and the 6-thioguanine-covered AuNP **4** significantly increase in the interaction energy also. In the meantime, neutral AuNPs **5** and **6** are effectively separated from each other, as reflected by the longer interparticle distances and low average number of particles in the selected areas. Each AuNP **6** particle is suggested to be isolated as a single dot due to effective hydrophobic repulsion. Thus, the values of the particle-to-particle interaction parameter ($\chi_{p\text{-}p}$) are high. Compared with the citrate-covered AuNP **1**, the charged ligands are observed to increase the interparticle attraction, while the neutral ligands generate effective repulsive energy.

Figure 2c presents the zone-plate X-ray nanoscopy (XN) images of the particles. XN is performed at the 1B2 beamline of the Pohang Accelerator Laboratory (Pohang, Korea). The detailed experimental setup is illustrated in Scheme 1. X-ray source radiates from a bending magnet of 2.5 GeV of Pohang Light Source (PLS) and then monochromatized using Ge(111) double-crystal monochromator (DCM). For the nanoscopy, 7 keV X-ray is nominally selected. Monochromatic

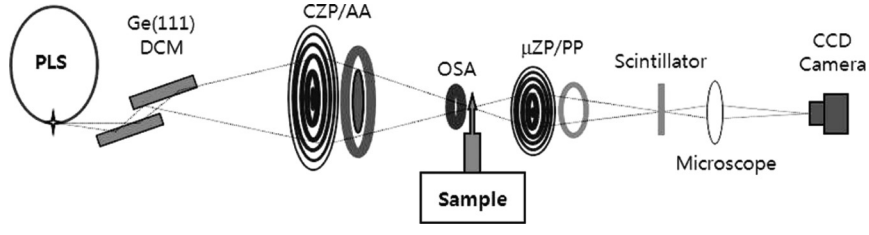

Scheme 1. Zone-plate X-ray nanoscopy (XN) setup.

X-ray is focused on the sample using a condenser zone-plate (CZP) with 4 and 100 nm in inner- and outermost diameter. To obtain a hollow-cone X-ray illuminating on a sample necessary for Zernike phase contrast imaging, a stainless steel annular ring of inner and outer diameters of 2.4 and 3.2 mm, respectively, is used (AA). An order sorting aperture (OSA) made of tungsten plate is used to pass the focused beam only to block other zeroth and higher order diffracted X-rays. Imaging zone-plate is fabricated with 1.6 μm thick gold zone rings on the 100 nm thick silicon nitride (Si_3N_4) membrane. Depth of focus of the objective zone-plate is 200 μm at 7 keV, limiting the practical thickness of the sample less than 200 μm. For phase contrast imaging, a gold-plated ring-shaped phase plate array is located downstream of the objective lens, and the ring dimensions (114.6 μm) are matched with that of the annular ring aperture (AA) located at the condenser zone-plate (CZP). Thicknesses of the phase plates (PP) are 0.7 μm, which correspond to λ/4 phase delay for positive phase contrast. Primary X-ray image is 50 times magnified by objective zone-plate lens and converted into a visible image on a thin scintillator crystal CsI(Tl). The visible image is further magnified by a 20× optical microscope, making total magnification 1000× on a cooled CCD camera. The camera (Princeton Instrument VersArray 1300B cooled CCD) with 1340 × 1300 pixels generates an equivalent field of view of 21 × 21 μm^2.

The X-ray absorptions of the AuNPs positioned over an X-ray-transparent silicon nitride (Si_3N_4) membrane are measured. The intensity values are subtracted by the background, and the standard deviations of the intensity fluctuations are obtained. From the peak-to-peak distances of the X-ray absorption profiles, the average sizes of the microscale clusters are obtained, as presented in Figure 2d. The figure also illustrates the number of clusters counted in each 3 × 3 μm^2 area. The average size and number of the clusters exhibit opposing trends. This indicates that the density of the AuNP is constant regardless of the cluster formation. The average sizes of the microscale clusters are inversely proportional to the submicrometer interparticle distance (d_{av}) previously observed in Figure 2b, wherein the close interparticle distance produces a small number of clusters with large size. It is interesting that AuNP **5** exhibits a rather smaller cluster in size even though the interparticle distance is large in Figure 2b. Due to the neutral feature of the functional group, AuNP **5** shows a higher interparticle repulsion, leading to a longer interparticle distance in nanoscale observed in Figure 2b. However, due to the hydrophilic nature of ethanol ligand in AuNP **5**, the clusters have adequate water solubility and a relatively small cluster in microscale observed in Figure 2d.

Dynamic X-ray Imaging of Sap Flow Using Surface-Modified AuNPs. Before being applied to the biosystem, the flow motions of the AuNPs are tested in the synchrotron X-ray imaging system. The flow motion of the concentration-controlled AuNP **5** caused by gravity is captured in Figure 3a as a function of time. The images are captured consecutively by the synchrotron X-ray source at the 7B2 beamline of the Pohang Accelerator Laboratory (Pohang, Korea).[13] Using a bending magnet, X-rays with a peak energy of 20.3 keV (8−30 keV range) are applied as a function of time without monochromator to obtain high energy. A $CdWO_4$ crystal is used as a scintillator to convert the X-ray into visible wavelength. A charge-coupled device (CCD) camera is used to convert the optical brightness into electrical signals. Time-resolved images are captured through the Kapton window covering a sample holder during the designed time interval at a speed rate of 25 frames per second. Starting from the concentration of 2.4 × 10^{18} AuNPs/m^3, the concentration of AuNP increases. When the particle concentration reaches 2.4 × 10^{19} AuNPs/m^3, proper flow images are successfully obtained due to proper cluster formation.

In this study, we aim to develop a methodology to use surface-modified AuNPs as particulate flow tracers in visualizing the uptake and transport of sap in xylem vessels of a plant in a dynamic way. To see through the plant tissues effectively and optimize the X-ray absorption efficiency of AuNPs under the given experimental conditions, monochromatic X-ray beam in the 10 KeV energy with 1% bandwidth is applied. The images are obtained at the 1B2 beamline of the Pohang Accelerator Laboratory. The X-ray source radiated from a bending magnet passes 200 sheets of W/B_4C (double multilayer monochromator) to narrow down the energy band. The size of the beam illuminating the test sample is adjusted using a slit module to avoid unnecessary exposure of the X-ray on the sample. Primary X-ray image is converted into a visible image on a thin scintillator crystal CsI(Tl). The visible X-ray images are captured using a cooled CCD camera (Redlake, Megaplus) with 1k × 1k pixel resolution. The field of view with a 10× objective lens in front of the camera is about 595 × 595 μm^2 in physical size.

Depending on the surface properties of the AuNPs designed in this study, specific surface modification enhances the accumulation at the specific part of the plants (data not shown here). The selective uptakes and accumulations can provide important information over the metabolic pathways and structural information which cannot be observed without flow tracers. Among the AuNPs designed in this study, AuNPs with hydrophobic character (AuNP **3** and AuNP **6**) interact with the secondary lateral cell walls of the xylem more effectively. This results in staining of cell walls by such AuNPs, which are especially useful in visualizing the xylem structure more clearly rather than allowing their use as flow tracers. The *in vivo* dynamic tracking of sap flow is limited in the current characteristics of synchrotron X-ray imaging. Indeed, the movement of air/water

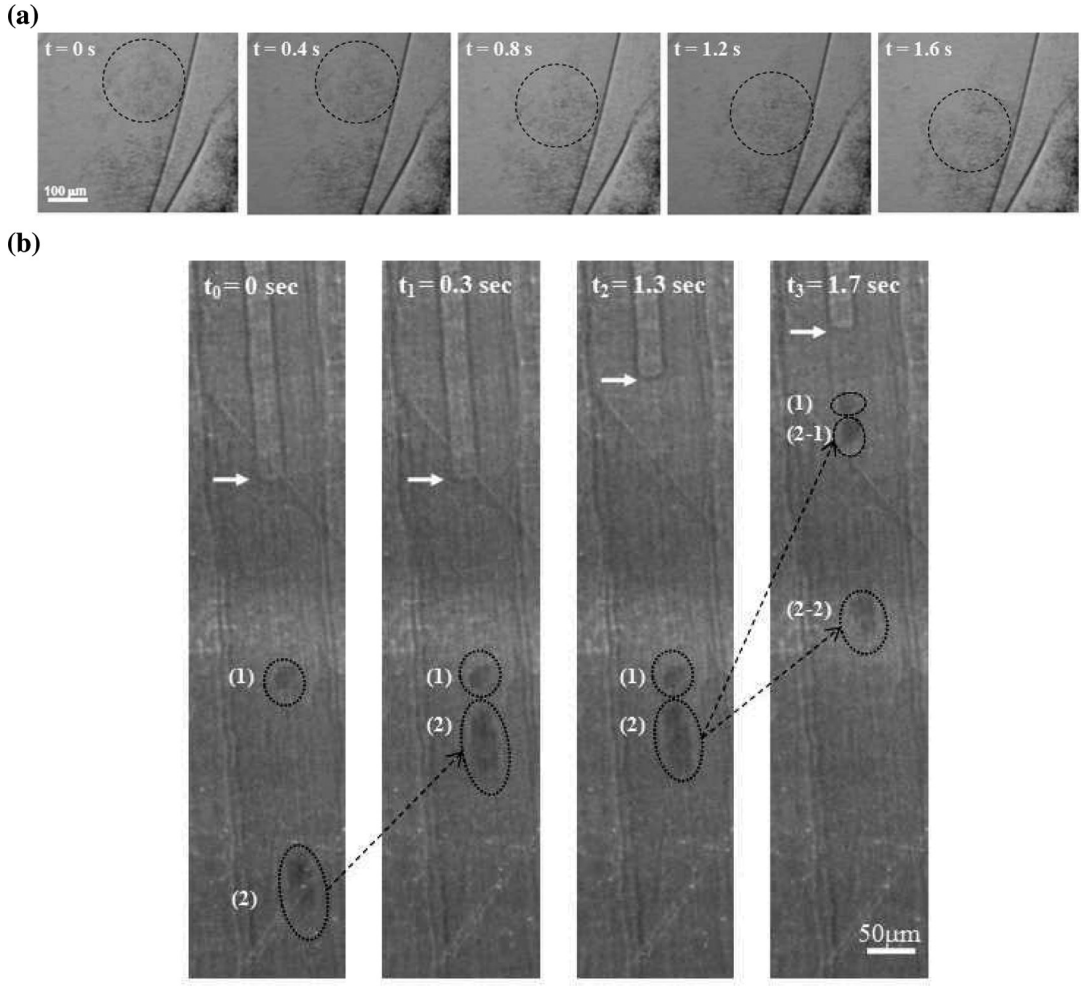

Figure 3. Application of AuNPs to the visualization of fluid dynamics in a living organism. (a) Time-dependent flow motions of the concentration-controlled AuNP 5 aqueous solution captured by X-ray imaging. (b) Four consecutive images showing the uptakes and transports of AuNP 5 inside the xylem vessels of a rice leaf sheath visualized by X-ray imaging. The arrow indicates the meniscus between water and air. (1) and (2) are the initial positions of AuNP 5 clusters in the sap. Between the images at $t_0 = 0$ and $t_0 = 0.3$ s, only cluster (2) moves upward. Meanwhile, from the images at $t_0 = 1.3$ and $t_0 = 1.7$ s, cluster (1) moves up, simultaneously, cluster (2) is separated into two distinct clusters (2−1) and (2−2) with different velocity. Video clip for the detailed real-time movement of the AuNP 5 clusters are available in the Supporting Information.

interfaces (menisci) during the refilling of dehydrated xylem vessels was used as an indirect flow tracer.[19] Therefore, the use of AuNPs as flow tracers opens a great possibility to track sap flow motions in intact plants. AuNP flow tracer could allow the direct evaluation of changes in flow characteristics especially when plants are under water stress.

The rice leaf sheath used in this study is first dried-up and then dipped in the selected AuNP solutions. By replacing the normal sap with the AuNP solutions, their successful uptake inside the xylem vessels of a rice leaf sheath is observed and illustrated in Figure 3b. Among the six surface-modified AuNPs in this study, the neutral and hydrophilic AuNP **5** at a controlled concentration was the most suitable to track the sap flow motion in real-time with minimized accumulation noticeable in this system. This can be supported by the unique physical properties of AuNP **5** with high hydrophilicity in microscale but effective aggregation in the aforementioned nanoscale. AuNP **5** was transported most effectively by passing through the perforated end walls of vessel elements (perforation plates). Due to high hydrophilicity, AuNP **5** is easily dissolved in the sap fluid that is mainly composed of water. Simultaneously, this AuNP **5** aqueous solution is taken up inside the xylem vessels during the refilling of dehydrated xylem vessels. The AuNP **5**, which aggregated physically at microscale, is detected by the synchrotron X-ray imaging system (the resolution is approximately 1 μm). The hydrophilic AuNP **5** shows a relatively stable behavior and forms clusters of various sizes.

In Figure 3b, the spots of (1) and (2) represent the position of the AuNP **5** at the beginning of the observed uptake. As the flow continues, the AuNPs positioned at (2) move faster while those at (1) remain stationary due to the resistances produced by a perforation plate crossing the vessels. However, at the time of 1.7 s, those at (1) overcome the flow resistance

and pass through the perforation plate. Because of insufficient pulling capacity in the xylem vessel, the AuNPs initially amassed at (2) divide into (2−1) and (2−2). A distant cluster of (2−1) then follows the (1) as time passes, while the movement of cluster (2−2) is delayed. Interestingly, the motion of this AuNPs is not identical to the movement of the air/water meniscus indicated by the white arrows at the upper part of the xylem vessels. There is a sudden uptake controlled by the speed of AuNP **5** movements, while the upper meniscus is stopped at a perforation plate directly. This shows the existence of radial water movement from adjacent xylem vessels. This type of monitoring provides new insights into the real-time visualization of axial and radial sap flows together. The typical imaging methods without a tracer cannot successfully visualize these kinds of phenomena.

The locally diversified flow motions of the AuNPs reflect the positional delay due to nonlinear flow character of the sap flow, which controls the complex life phenomena of the rice. The local delivery of the sap flow represented by AuNP **5** in this system shows dynamic and selective uptake of the sap flow. The paths wetted by the AuNP solutions reflect the basic structure of the vessels, which mainly transport the flow, protecting the plants from the withering out. However, depending on the number of pathways branched out, the pressure gradient loaded on the specific parts of the rice leaf is successfully observed with the help of AuNP **5** in this system, where the flow motion is locally diversified. This is one of the unique roles of AuNP flow sensors because only selective visualization of the flows can explain the differentiated flow pathways from the original sap and newly introduced sap flow. In addition, due to important role of the pit membrane crossing each xylem vessel, the regional pressure gradients are successfully detected by this AuNP **5** solution. This result successfully explains the filling−refilling process of the rice leaf, the local pressure gradient, and flow velocities.

CONCLUSIONS

Particle-traced X-ray imaging technique allows us to quantify the transport of sap inside the xylem vessels marked by the AuNPs aggregated in microscale and simultaneously spread in nanoscale. By visualizing the transport of water through the perforation plates tracked by the surface-modified AuNPs as a smart flow tracer, study of the relationships between the morphology of xylem vessels and sap transport is possible. This experimental technique can be further developed and contribute to solving the still unraveled secrets on the metabolism of plants. We found that the physical properties of the designed AuNPs (especially, the surface modification) strongly contribute to the efficacy of the imaging and the interaction with the observed biofluids.

Acknowledgment. This work was supported by the Creative Research Initiatives (Center for Biofluid and Biomimic Research) from the Ministry of Education, Science and Technology (MEST) and from the National Research Foundation (NRF) of Korea. The authors thank for the valuable help with the X-ray imaging experiments performed at 1B2 and 7B2 beamlines of Pohang Accelerator Laboratory (PAL) (Pohang, Korea).

Supporting Information Available: Detailed real-time movement of the AuNP **5** clusters. This material is available free of charge *via* the Internet at http://pubs.acs.org.

REFERENCES AND NOTES

1. Marshall, E. Metabolic Research: Canadian Group Claims 'Unique' Database. *Science* **2007**, *315*, 583–584.
2. De Melis, M.; Morbiducci, U.; Scalise, L.; Tomasini, E. P.; Delbeke, D.; Baets, R.; Van Bortel, L. M.; Segers, P. Noncontact Approach for the Evaluation of Large Artery Stiffness: A Preliminary Study. *Am. J. Hypertens.* **2008**, *21*, 1280–1283.
3. Westneat, M. W.; Betz, O.; Blob, R. W.; Fezzaa, K.; Cooper, W. J.; Lee, W. K. Tracheal Respiration in Insects Visualized with Synchrotron X-ray Imaging. *Science* **2003**, *299*, 558–560.
4. Tsai, W. L.; Hsu, P. C.; Hwu, Y.; Chen, C. H.; Chang, L. W.; Je, J. H.; Lin, H. M.; Groso, A.; Margaritondo, G. Electrochemistry: Building on Bubbles in Metal Electrodeposition. *Nature* **2002**, *417*, 139.
5. Lee, S. J.; Kim, G. B.; Yim, D. H.; Jung, S. Y. Development of a Compact X-ray Particle Image Velocimetry for Measuring Opaque Flows. *Rev. Sci. Instrum.* **2009**, *80*, 033706.
6. Fouras, A.; Dusting, J.; Lewis, R.; Hourigan, K. Three-Dimensional Synchrotron X-ray Particle Image Velocimetry. *J. Appl. Phys.* **2007**, *102*, 064916.
7. http://physics.nist.gov/PhysRefData/XrayMassCoef.
8. Choi, H. S.; Liu, W.; Misra, P.; Tanaka, E.; Zimmer, J. P.; Ipe, B. I.; Bawendi, M. G.; Frangioni, J. V. Renal Clearance of Quantum Dots. *Nat. Biotechnol.* **2007**, *25*, 1165–1170.
9. Shukla, R.; Bansal, V.; Chaudhary, M.; Basu, A.; Bhonde, R. R.; Sastry, M. Biocompatibility of Gold Nanoparticles and Their Endocytotic Fate Inside the Cellular Compartment: A Microscopic Overview. *Langmuir* **2005**, *21*, 10644–10654.
10. Link, S.; El-Sayed, M. A. Spectral Properties and Relaxation Dynamics of Surface Plasmon Electronic Oscillations in Gold and Silver Nanodots and Nanorods. *J. Phys. Chem. B* **1999**, *103*, 8410–8426.
11. Lee, J.-S.; Ulmann, P. A.; Han, M. S.; Mirkin, C. A. A DNA−Gold Nanoparticle-Based Colorimetric Competition Assay for the Detection of Cysteine. *Nano Lett.* **2008**, *8*, 529–533.
12. Sokolov, K.; Follen, M.; Aaron, J.; Pavlova, I.; Malpica, A.; Lotan, R.; Richards-Kortum, R. Real-Time Vital Optical Imaging of Precancer Using Anti-Epidermal Growth Factor Receptor Antibodies Conjugated to Gold Nanoparticles. *Cancer Res.* **2003**, *63*, 1999–2004.
13. Lee, S. J.; Jung, S. Y.; Ahn, S. Flow Tracing Microparticle Sensors Designed for Enhanced X-ray Contrast. *Biosens. Bioelectron.* **2010**, *25*, 1571–1578.
14. Nel, A. E.; Mädler, L.; Velegol, D.; Xia, T.; Hoek, E. M. V.; Somasundaran, P.; Klaessig, F.; Castranova, V.; Thompson, M. Understanding Biophysicochemical Interactions at the Nano-Bio Interface. *Nat. Mater.* **2009**, *8*, 543–557.
15. Li, M.; Schnablegger, H.; Mann, S. Coupled Synthesis and Self-Assembly of Nanoparticles To Give Structures with Controlled Organization. *Nature* **1999**, *402*, 393–395.
16. Akbulut, M.; Alig, A. R. G.; Min, Y.; Belman, N.; Reynolds, M.; Golan, Y.; Israelachvili, J. Forces between Surfaces across Nanoparticle Solutions: Role of Size, Shape, and Concentration. *Langmuir* **2007**, *23*, 3961–3969.
17. Tyree, M. T. The Cohesion-Tension Theory of Sap Ascent: Current Controversies. *J. Exp. Bot.* **1997**, *48*, 1753–1765.
18. Zimmermann, U.; Schneider, H.; Wegner, L. H.; Haase, A.

Water Ascent in Tall Trees: Does Evolution of Land Plants Rely on a Highly Metastable State? *New Phytol.* **2004**, *162*, 575–615.
19. Lee, S.-J.; Kim, Y. *In Vivo* Visualization of the Water-Refilling Process in Xylem Vessels Using X-ray Micro-imaging. *Ann. Bot.* **2008**, *101*, 595–602.
20. Shane, M. W.; McCully, M. E.; Canny, M. J. Architecture of Branch-Root Junctions in Maize: Structure of the Connecting Xylem and the Porosity of Pit Membranes. *Ann. Bot.* **2000**, *85*, 613–624.
21. Gasco, A.; Nardini, A.; Gortan, E.; Salleo, S. Ion-Mediated Increase in the Hydraulic Conductivity of Laurel Stems: Role of Pits and Consequences for the Impact of Cavitation on Water Transport. *Plant Cell Environ.* **2006**, *29*, 1946–1955.
22. Corredor, E.; Testillano, P. S.; Coronado, M.-J.; González-Melendi, P.; Fernández-Pacheco, R.; Marquina, C.; Ibarra, M. R.; de la Fuente, J. M.; Rubiales, D.; Pérez-de-Luque, A.; Risueño, M.-C. A Set of EST-SNPs for Map Saturation and Cultivar Identification in Melon. *BMC Plant Biol.* **2009**, *9*, 90.
23. Hostetler, M. J.; Stokes, J. J.; Murray, R. W. Infrared Spectroscopy of Three-Dimensional Self-Assembled Monolayers: *N*-Alkanethiolate Monolayers on Gold Cluster Compounds. *Langmuir* **1996**, *12*, 3604–3612.
24. Brust, M.; Walker, M.; Bethell, D.; Schiffrin, D. J.; Whyman, R. J. Synthesis of Thiol-Derivatised Gold Nanoparticles in a Two-Phase Liquid−Liquid System. *J. Chem. Soc., Chem. Commun.* **1994**, 801–802.
25. Turkevitch, J.; Stevenson, P. C.; Hillier, J. A Study of the Nucleation and Growth Processes in the Synthesis of Colloidal Gold. *Discuss. Faraday Soc.* **1951**, *11*, 55–75.
26. Yonezawa, T.; Kunitake, T. Practical Preparation of Anionic Mercapto Ligand-Stabilized Gold Nanoparticles and Their Immobilization. *Colloids Surf. A* **1999**, *149*, 193–199.
27. Hamaker, H. C. The London-van der Waals Attraction between Spherical Particles. *Physica* **1937**, *4*, 1058–1072.
28. Logunov, S. L.; Ahmadi, T. S.; El-Sayed, M. A.; Khoury, J. T.; Whetten, R. L. Electron Dynamics of Passivated Gold Nanocrystals Probed by Subpicosecond Transient Absorption Spectroscopy. *J. Phys. Chem. B* **1997**, *101*, 3713–3719.
29. Templeton, A. C.; Pietron, J. J.; Murray, R. W.; Mulvaney, P. Solvent Refractive Index and Core Charge Influences on the Surface Plasmon Absorbance of Alkanethiolate Monolayer-Protected Gold Clusters. *J. Phys. Chem. B* **2000**, *104*, 564–570.
30. Su, K.-H.; Wei, Q.-H.; Zhang, X.; Mock, J. J.; Smith, D. R.; Schulz, S. Interparticle Coupling Effects on Plasmon Resonances of Nanogold Particles. *Nano Lett.* **2003**, *3*, 1087–1090.
31. Mie, G. Beiträge zur Optik trüber Medien, Speziell Kolloidaler Metallösungen. *Ann. Phys.* **1908**, *25*, 377–445.
32. Swanson, N. L.; Billard, B. D. Optimization of Extinction from Surface Plasmon Resonances of Gold Nanoparticles. *Nanotechnology* **2003**, *14*, 353.
33. Serjeant, E. P., Dempsey, B., Eds. *Ionization Constants of Organic Acids in Solution, IUPAC Chemical Data Series No. 23*; Pergamon Press: Oxford, UK, 1979.
34. http://www.chemicalbook.com/ProductMSDSDetailCB6361837_EN.htm.
35. Evans, D. F.; Wennerström, H. *The Colloidal Domain*; VCH Publishers, Inc: New York, 1994.
36. Youn, H. S.; Jung, S.-W. Hard X-ray Microscopy with Zernike Phase Contrast. *J. Microsc.* **2006**, *223*, 53–56.